Technische Universität Graz

Shape Optimization of Rotating Electric Machines using Isogeometric Analysis and Harmonic Stator-Rotor Coupling

M. Merkel, P. Gangl and S. Schöps

Berichte aus dem Institut für Angewandte Mathematik

Bericht 2019/3

Technische Universität Graz

Shape Optimization of Rotating Electric Machines using Isogeometric Analysis and Harmonic Stator-Rotor Coupling

M. Merkel, P. Gangl and S. Schöps

Berichte aus dem
Institut für Angewandte Mathematik

Bericht 2019/3

Technische Universität Graz
Institut für Angewandte Mathematik
Steyrergasse 30
A 8010 Graz

WWW: `http://www.applied.math.tugraz.at`

Shape Optimization of Rotating Electric Machines using Isogeometric Analysis and Harmonic Stator-Rotor Coupling

Melina Merkel[1,2], Peter Gangl[3] and Sebastian Schöps[1,2]
[1]Institut für Teilchenbeschleunigung und Elektromagnetische Felder (TEMF), Technische Universität Darmstadt, Germany
[2]Centre for Computational Engineering, Technische Universität Darmstadt, Germany
[3]Institut für Angewandte Mathematik, Technische Universität Graz, Austria

This work deals with shape optimization of electric machines using isogeometric analysis. Isogeometric analysis is particularly well suited for shape optimization as it allows to easily modify the geometry without remeshing the domain. A 6-pole permanent magnet synchronous machine is modeled using a multipatch isogeometric approach and rotation of the machine is realized by modeling the stator and rotor domain separately and coupling them at the interface using harmonic basis functions. Shape optimization is applied to the model minimizing the total harmonic distortion of the electromotive force as a goal functional.

***Index Terms*—electric machines, harmonic stator-rotor coupling, isogeometric analysis, shape optimization**

I. Introduction

As a result of the energy transition, the simulation of electromechanical energy converters, in particular electric machines, is becoming increasingly important to obtain efficient and robust designs. Commonly, a workflow based on analytical estimates and the Finite Element Method (FEM) is used for 2D and finally 3D domains. In most classical approaches, the geometry is only approximated, e.g., with an accuracy that depends on the mesh refinement. These errors can be avoided when using Isogeometric Analysis (IGA) [1], [2], [3], [4] which uses B-splines and/or Non-Uniform Rational B-splines (NURBS) as basis for geometry and solution space. In IGA, the geometry can be easily and smoothly transformed by moving the control points of the splines such that there is no need to remesh the domain when the geometry is modified. This makes IGA very well suited for shape optimization [5]. Numerical optimization based on magnetic equivalent circuits or finite element models has lead to large improvements in the designs of technical applications, e.g., of permanent magnet synchronous machines. During the last 30 years there has been a lot of research on finite element based optimization methods (see, e.g., [6], [7] and the references therein). Originally, mainly gradient-based optimization methods were used (see, e.g., [8, 9, 10]) but stochastic optimization algorithms became more popular during the last 20 years (see, e.g., [11], [12]). Most of the proposed algorithms use stochastic or population-based optimization, e.g., genetic algorithms and particle swarm optimization (see, e.g., [13]) which have also been extended to multi-objective optimization problems (see, e.g., [14, 15]). For permanent magnet synchronous machines, stochastic optimization methods are commonly used (see, e.g.,[16, 17, 18]).

This contribution deals for the first time with shape optimization of a rotating electrical machine discretized with IGA. We use shape calculus to obtain shape derivatives such that gradient-based optimization becomes feasible. The rotor and stator domains are discretized separately and are coupled using harmonic stator-rotor coupling [19].

The paper is structured as follows: In Section II the model of the electric machine and its quantities of interest are introduced. We introduce the shape optimization problem and derive the formula of the shape derivative using shape calculus in Section III. In Section IV the discretization of the machine using harmonic stator-rotor coupling and isogeometric analysis is explained and the resulting saddle-point problem is presented. We conclude the paper by explaining our gradient-based shape optimization algorithm and present numerical results for the minimization of the total harmonic distortion of the electromotive force in Section V.

II. Model of the Electric Machine

Electromagnetic phenomena are described by Maxwell's equations. For many applications it is sufficient to consider the magnetostatic approximation in a working point, i.e., neglecting displacement and eddy currents and non-linearity of the materials. In a domain $D_{3\mathrm{D}}$ the magnetostatic formulation of Maxwell's equations is given by

$$\nabla \times (\nu \nabla \times \mathbf{A}) = \mathbf{J}_{\mathrm{src}} + \nabla \times \mathbf{M}, \tag{1}$$

with the piecewise constant reluctivity ν, the magnetic vector potential $\mathbf{A}$, the current density $\mathbf{J}_{\mathrm{src}} = \sum_k \boldsymbol{\chi}_k i_k$ given by winding functions $\boldsymbol{\chi}_k$ and currents i_k [20], the magnetization of the permanent magnets $\mathbf{M}$ and homogeneous Dirichlet boundary conditions $\mathbf{A} \times \mathbf{n} = 0$ on $\partial D_{3\mathrm{D}}$, where $\mathbf{n}$ is the normal vector. The source current density $\mathbf{J}_{\mathrm{src}}$ and the permanent magnetization $\mathbf{M}$ vanish outside the coil (D_{c}) and permanent magnet (D_{pm}) regions, respectively, see Fig. 1. A common quantity of interest when designing electric machines is the total harmonic distortion (THD) of the electromotive force (EMF) $\mathcal{E}$. The total harmonic distortion of a function $f = f(t)$ is defined as

$$\mathrm{THD}_{\mathcal{I}}(f) = \frac{\sqrt{\sum_{n \in \mathcal{I}, n \neq 1} |c_n|^2}}{|c_1|}, \tag{2}$$

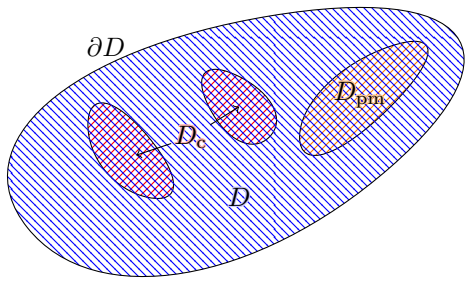

Fig. 1: Example for a domain D with coil region D_{c}, permanent magnet region D_{pm} and domain boundary ∂D.

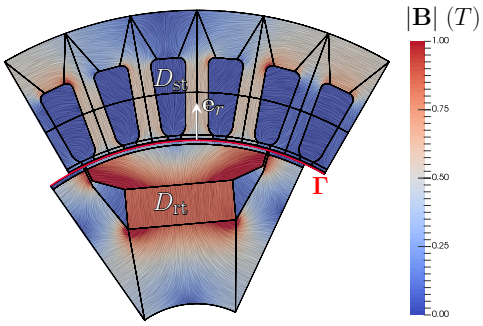

Fig. 2: Multipatch model of one pole of a 6-pole permanent magnet synchronous machine. The magnetic flux density $\mathbf{B}$ is shown which was computed using isogeometric analysis.

where c_n are the coefficients of the Fourier series of $f(t)$, i.e.

$$f(t) = \sum_{n=-\infty}^{\infty} c_n e^{\imath n t}, \tag{3}$$

and $\mathcal{I} \subset \mathbb{N}$ is an index set of frequencies to consider, e.g., one may disregard frequencies that cannot be diminished by shape optimization. Alternatively, the expansion (3) can be written as

$$f(t) = \frac{A_0}{2} + \sum_{n=1}^{\infty} A_n \cos(nt) + B_n \sin(nt)$$

with coefficients $A_n = c_n + c_{-n}$ for $n \geq 0$ and $B_n = \imath(c_n - c_{-n})$ for $n \geq 1$. Note that it holds that $|c_n| = \sqrt{A_n^2 + B_n^2}/2$. Using these coefficients, the THD can be written as

$$\mathrm{THD}(f) = \sqrt{\frac{\sum_{n\in\mathcal{I}, n\neq 1} A_n^2 + B_n^2}{A_1^2 + B_1^2}}. \tag{4}$$

We are interested in the THD of the EMF. Therefore, the amplitudes c_n are obtained by Fourier analysis of the voltages

$$\mathcal{E}_k(\mathbf{A}(t)) = \partial_t \Psi_k(\mathbf{A}(t)), \tag{5}$$

with the flux linkage

$$\Psi_k(\mathbf{A}(t)) = N_p \int_{D_{3\mathrm{D}}} \boldsymbol{\chi}_k \cdot \mathbf{A}(t) \,\mathrm{d}D_{3\mathrm{D}}, \tag{6}$$

where N_p is the number of pole pairs. The voltages $\mathcal{E}_k$ are induced by the electromagnetic force in the windings under the assumption that the coils of the poles are connected in series.

In the planar 2D case (1) is considered on a cross section $D \subset \mathbb{R}^2$ and reduces to

$$-\nabla \cdot (\nu \nabla u) = J_{\mathrm{src},z} + \nabla \times \mathbf{M} \cdot \mathbf{e}_z, \tag{7}$$

where $u(x, y)$ is the z-component of the magnetic vector potential $\mathbf{A} = [0, 0, u]^\top$, $J_{\mathrm{src},z} = \sum_k \chi_k i_k$ is the z-component of the current density given by winding functions χ_k and currents i_k and $\mathbf{e}_z$ is the unit vector in z-direction.

III. Optimization

A. Problem statement

We want to optimize the $2D$ shape Ω of the 3-phase permanent magnet synchronous machine from Fig. 2, which has $N_p = 3$ pole pairs, in terms of the total harmonic distortion (THD) of the electromotive force (EMF) as introduced in (5). Due to periodicity of the stator windings, we will restrict ourselves to the optimization of the first voltage and set $\mathcal{E} := \mathcal{E}_1$ and $\chi = \chi_1$. Note the dependence of $\mathcal{E}$ on the shape Ω via the solution u to (7), i.e., $\mathcal{E} = \mathcal{E}(u(t, \Omega))$. Thus, we consider the optimization problem

$$\min_{\Omega\in\mathcal{A}} \mathcal{J}(\Omega) := \mathrm{THD}_{\mathcal{I}}(\mathcal{E}(u(t, \Omega))), \tag{8}$$

that is constrained by the machine model (7), which, for $t \in [0, T]$, reads in its weak form: Find $u = u(\alpha(t))$ such that

$$\underbrace{\int_D \nu_\Omega(\alpha(t)) \nabla u \cdot \nabla v \,\mathrm{d}D}_{=:a[\alpha(t)](\Omega;u,v)} = \langle r(t, \alpha(t)), v\rangle \tag{9}$$

for all test functions v. Here $T = 2\pi/\omega$ is the (electrical) period length, $\alpha(t)$ the rotor angle, which may be given by the equation of motion. We allow all geometries from an admissible set $\mathcal{A}$. Both u and v satisfy homogeneous Dirichlet boundary conditions on the inner and outer circular parts of the boundary and periodic boundary conditions on the left and right parts. Finally, the right-hand-side is given by

$$\begin{aligned}\langle r(t,\alpha(t)), v\rangle = &\int_{D_{\mathrm{c}}} \sum_{k=1}^{3} \chi_k(x, y) i_k(t)\, v(x, y) \,\mathrm{d}D_{\mathrm{c}} \\ &+ \int_{D_{\mathrm{pm}}(\alpha(t))} \begin{pmatrix} -M_2 \\ M_1 \end{pmatrix} \cdot \nabla v(x, y) \,\mathrm{d}D_{\mathrm{pm}}(\alpha(t))\end{aligned} \tag{10}$$

and contains the excitations due to permanent magnets and the coils. Here, M_1 and M_2 are the first and second component of the magnetization vector $\mathbf{M}$, respectively, $D_{\mathrm{pm}}(\alpha(t))$ denotes the permanent magnet region after rotation by the angle $\alpha(t)$ and we exploit for a more compact notation that the permanent magnets lie in the rotating part and the coils in the stator. We indicate the dependence of the reluctivity function on the current shape Ω which is subject to the shape optimization by writing ν_Ω.

Moreover, we introduce a temporal discretization $\{t_1, \ldots, t_{N_\alpha}\}$ into $N_\alpha = 120$ points in time and a corresponding discretization of the range of angular displacements into N_α rotor positions, $\boldsymbol{\alpha} := (\alpha_1, \ldots, \alpha_{N_\alpha})$. For $j \in \{1, \ldots, N_\alpha\}$ and a given shape Ω, let $a_j(\Omega; \cdot, \cdot) := a[\alpha_j](\Omega; \cdot, \cdot)$ and $r_j := r(t_j, \alpha_j)$ according

to the definitions in (9) and (10), respectively. Approximating $u(t,\Omega)$ for $t \in [0,T]$ by $\{u_1,\dots,u_{N_\alpha}\}$ and introducing the notation $\mathcal{J}(u_1,\dots,u_{N_\alpha}) := \mathrm{THD}_{\mathcal{I}}(\mathcal{E}(u_1,\dots,u_{N_\alpha}))$, problem (8)–(9) after discretization with respect to rotor positions can be written as the optimization problem

$$\min_{\Omega} \mathcal{J}(u_1,\dots,u_{N_\alpha}) \tag{11}$$

$$\text{s.t.} \begin{cases} a_1(\Omega;u_1,v_1) = \langle r_1,v_1\rangle \ \forall v_1, \\ \vdots \\ a_{N_\alpha}(\Omega;u_{N_\alpha},v_{N_\alpha}) = \langle r_{N_\alpha},v_{N_\alpha}\rangle \ \forall v_{N_\alpha}, \end{cases} \tag{12}$$

which is constrained by N_α boundary value problems corresponding to the N_α rotor positions under consideration.

B. Shape Sensitivity Analysis

The shape derivative $d\mathcal{J}(\Omega;\mathbf{W})$ of a domain-dependent functional $\mathcal{J} = \mathcal{J}(\Omega)$ represents the sensitivity of the functional with respect to a perturbation of the domain in the direction of a given vector field $\mathbf{W}$. The shape derivative is defined as

$$d\mathcal{J}(\Omega;\mathbf{W}) = \lim_{\delta \searrow 0} \frac{\mathcal{J}(T_\delta^{\mathbf{W}}(\Omega)) - \mathcal{J}(\Omega)}{\delta}, \tag{13}$$

if this limit exists and the mapping $\mathbf{W} \mapsto d\mathcal{J}(\Omega;\mathbf{W})$ is linear and continuous on the space of smooth vector fields. Here, $T_\delta^{\mathbf{W}}$ represents a transformation which moves every point $\mathbf{x}$ a distance $\delta > 0$ in the direction given by the vector field $\mathbf{W}$, $T_\delta^{\mathbf{W}}(\mathbf{x}) = \mathbf{x} + \delta\mathbf{W}(\mathbf{x})$.

For deriving the shape derivative $d\mathcal{J}(\Omega;\mathbf{W})$ for the optimization problem (11)–(12), we follow the steps taken in [21]. First, we introduce the Lagrangian

$$\mathcal{L}(\Omega,\varphi_1,\dots,\varphi_{N_\alpha},\psi_1,\dots,\psi_{N_\alpha}) := \mathcal{J}(\varphi_1,\dots,\varphi_{N_\alpha}) + \sum_{k=1}^{N_\alpha} \left(a_k(\varphi_k,\psi_k) - \langle r_k,\psi_k\rangle\right).$$

For ease of notation, we will use the notation $\mathbf{u} = (u_1,\dots,u_{N_\alpha})$ and similar for other quantities. Note that, for u_i satisfying the i-th equation of (12), it holds that

$$\frac{\partial}{\partial\psi_i}\mathcal{L}(\Omega,\mathbf{u},\boldsymbol{\psi})(q_i) = a_i(u_i,q_i) - \langle r_i,q_i\rangle = 0$$

for any test function q_i. Similarly, we introduce the adjoint states p_i, $i = 1,\dots,N_\alpha$, as the solutions to

$$0 = \frac{\partial}{\partial\varphi_i}\mathcal{L}(\Omega,\mathbf{u},\mathbf{p})(v_i) = \frac{\partial\mathcal{J}}{\partial\varphi_i}(\mathbf{u})(v_i) + a_i(v_i,p_i) \tag{14}$$

for all test functions v_i.

Let us now consider the functional $\mathcal{J} = \mathcal{J}(u_1,\dots,u_{N_\alpha})$ more closely. We will use the representation (4) for the THD. Let $(C_n)_{n\in\mathcal{I}}$ the Fourier coefficients of the function $\Psi(u_1,\dots,u_{N_\alpha})$, i.e.,

$$\Psi(u_1,\dots,u_{N_\alpha}) = \sum_{n=-N_\alpha}^{N_\alpha} C_n e^{\imath nt}. \tag{15}$$

Using the Fourier representation (15) of the flux linkage and (5), the electromotive force can be written as

$$\mathcal{E}(u_1,\dots,u_{N_\alpha}) = \sum_{n=-N_\alpha}^{N_\alpha} \underbrace{\imath n C_n}_{c_n} e^{\imath nt}, \tag{16}$$

where $(c_n)_{n\in\mathcal{I}}$ are the Fourier coefficients of the electromotive force $\mathcal{E}$. This Fourier series can be rewritten as

$$\mathcal{E}(u_1,\dots,u_{N_\alpha}) = \frac{A_0}{2} + \sum_{n=1}^{N_\alpha} A_n\cos(nt) + B_n\sin(nt). \tag{17}$$

The coefficients A_n and B_n of the Fourier representation of $\partial_t\Psi$ (17) are obtained by time derivation and Fourier transform, which we will denote by $A_n = [\mathcal{F}'_a(\Psi(u_1,\dots,u_{N_\alpha}))]_n$ and $B_n = [\mathcal{F}'_b(\Psi(u_1,\dots,u_{N_\alpha}))]_n$, respectively. Exploiting the linearity of the discrete Fourier transform, the vectors $\mathbf{A}$ and $\mathbf{B}$ can also be written in terms of transformation matrices $\mathbf{M}_a = \mathcal{F}'_a(\mathbf{I})$ and $\mathbf{M}_b = \mathcal{F}'_b(\mathbf{I})$, where $\mathbf{I}$ is the identity matrix, i.e.,

$$A_k(u_1,\dots,u_{N_\alpha}) = \sum_{j=1}^{N_\alpha}\left((\mathbf{M}_a)_{k,j}\, N_p l_z \int_D \chi u_j \,\mathrm{d}D\right), \tag{18}$$

$$B_k(u_1,\dots,u_{N_\alpha}) = \sum_{j=1}^{N_\alpha}\left((\mathbf{M}_a)_{k,j}\, N_p l_z \int_D \chi u_j \,\mathrm{d}D\right), \tag{19}$$

where l_z is the length of the machine in z-direction.

In order to solve the adjoint state equation (14), we need to differentiate the functional $\mathcal{J} = \mathrm{THD}(\mathcal{E}(u_1,\dots,u_{N_\alpha}))$ with respect to u_i for $i \in \{1,\dots,N_\alpha\}$. Using the relation (4), we get

$$\frac{d\ \mathrm{THD}(\mathcal{E}(\mathbf{u}))}{du_i}(\mathbf{u})(v_i) = \frac{1}{\sqrt{A_1^2+B_1^2}} \frac{1}{\sqrt{\sum_{k\in\mathcal{I},k\neq 1} A_k^2+B_k^2}} \left(\sum_{k\in\mathcal{I},k\neq 1} A_kA'_k + B_kB'_k\right) - \frac{1}{(A_1^2+B_1^2)^{3/2}} \left(\sqrt{\sum_{k\in\mathcal{I},k\neq 1} A_k^2+B_k^2}\,(A_1A'_1+B_1B'_1)\right).$$

Here, we used the abbreviations $A'_k := \frac{dA_k}{du_i}(\mathbf{u})(v_i)$ and $B'_k := \frac{dB_k}{du_i}(\mathbf{u})(v_i)$. It can be seen from (18) and (19) that

$$\frac{dA_k}{du_i}(\mathbf{u})(v_i) = (\mathbf{M}_a)_{k,i}\, N_p l_z \int_D \chi v_i \,\mathrm{d}D,$$
$$\frac{dB_k}{du_i}(\mathbf{u})(v_i) = (\mathbf{M}_b)_{k,i}\, N_p l_z \int_D \chi v_i \,\mathrm{d}D.$$

Given the solutions to the forward problem (9) for all rotor positions $l \in \{1,\dots N_\alpha\}$, we obtain for the adjoint problem (14) defining the adjoint variable at rotor position $l \in \{1,\dots N_\alpha\}$: Find p_i such that

$$a_i(v_i,p_i) = -\frac{d\ \mathrm{THD}(\mathcal{E}(\mathbf{u}))}{du_i}(\mathbf{u})(v_i)$$

for all test functions v_i.

Finally, in a similar way as it was proposed in [21], assuming that the deformation vector field $\mathbf{W}$ vanishes on the interface

Γ and on the stator, and that the permanent magnet region remains unchanged, we obtain the formula for the shape derivative in the direction of a smooth vector field $\mathbf{W} \in C^1(D, \mathbb{R}^2)$:

$$d\mathcal{J}(\Omega; \mathbf{W}) = \sum_{l=1}^{N_\alpha} \int_{\Omega_{\mathrm{pm}}} (\nabla \cdot (\mathbf{W})\mathbf{I} - \mathbf{D}\mathbf{W}^\top)\nabla p_l \cdot \begin{pmatrix} -M_2 \\ M_1 \end{pmatrix} \mathrm{d}x + \sum_{l=1}^{N_\alpha} \int_D \nu \left(\nabla \cdot \mathbf{W}\,\mathbf{I} - \mathbf{D}\mathbf{W}^\top - \mathbf{D}\mathbf{W}\right)\nabla u_l \cdot \nabla p_l \,\mathrm{d}x. \tag{20}$$

Here, $\mathbf{I} \in \mathbb{R}^{2\times 2}$ denotes the two-dimensional identity matrix.

IV. Solution of the Forward Problem by IGA

In this section, we will treat the numerical solution of the forward problem (7) using Isogeometric Analysis and harmonic stator-rotor coupling allowing for a flexible treatment of the rotation.

A. Harmonic Stator-Rotor Coupling

As proposed in [19], stator and rotor domains D_q, where $q \in \{\mathrm{st}, \mathrm{rt}\}$ distinguishes between stator and rotor and $\overline{D} = \overline{D}_{\mathrm{rt}} \cup \overline{D}_{\mathrm{st}}$, are considered separately. They are coupled at the stator-rotor interface $\Gamma = \overline{D}_{\mathrm{rt}} \cap \overline{D}_{\mathrm{st}}$ in the air gap by enforcing the continuity of the magnetic vector potential u and of the azimuthal component of the magnetic field strength $H_\theta^{(\mathrm{st})}|_\Gamma(\theta_{\mathrm{st}}) = H_\theta^{(\mathrm{rt})}|_\Gamma(\theta_{\mathrm{rt}})$, where θ_{st} and θ_{rt} are the angular coordinates attached to stator and rotor domain, respectively. The angular displacement between the domains is $\alpha = \theta_{\mathrm{st}} - \theta_{\mathrm{rt}}$. In its weak form the problem (7) can be formulated as:

Find $(u_{\mathrm{st}}, u_{\mathrm{rt}}, \lambda) \in V_{\mathrm{st}} \times V_{\mathrm{rt}} \times \Lambda$ such that

$$\sum_q \int_{D_q} \nu_q \nabla u_q \cdot \nabla v_q \,\mathrm{d}\, D_q + \int_\Gamma \lambda \,[\![v]\!]\,\mathrm{d}\,\Gamma = \sum_q \langle r_q, v_q\rangle$$

with interface condition

$$\int_\Gamma [\![u]\!]\,\mu \,\mathrm{d}\,\Gamma = 0,$$

for all $v_q \in V_q$ and $\mu \in \Lambda$, $q \in \{\mathrm{st}, \mathrm{rt}\}$, where V_q are suitable function spaces which contain the necessary Dirichlet boundary conditions, v_q are the test functions, and r_q, $q \in \{\mathrm{st}, \mathrm{rt}\}$ are the contributions of the right hand side on the stator and rotor as in (10),

$$\langle r_{\mathrm{st}}, v_{\mathrm{st}}\rangle = \int_{D_{\mathrm{c}}} \sum_k \chi_k(x,y) i_k(t)\, v_{\mathrm{st}}(x,y)\,\mathrm{d}D_{\mathrm{c}}, \tag{21}$$

$$\langle r_{\mathrm{rt}}, v_{\mathrm{rt}}\rangle = \int_{D_{\mathrm{pm}}(\alpha)} \begin{pmatrix} -M_2 \\ M_1 \end{pmatrix} \cdot \nabla v(x,y)\,\mathrm{d}D_{\mathrm{pm}}(\alpha). \tag{22}$$

Moreover, $[\![v]\!] = (v_{\mathrm{st}} - v_{\mathrm{rt}})|_\Gamma$ denotes the jump of v across the interface Γ and $\lambda = \nu \nabla u^{(\mathrm{st})} \cdot \mathbf{e}_r = \nu \nabla u^{(\mathrm{rt})} \cdot \mathbf{e}_r = H_\theta^{(q)}$, where $\mathbf{e}_r$ is the unit vector in radial direction, is the θ-component of the magnetic field at the interface and can be interpreted as a Lagrange multiplier [22].

B. Discretization

The z-component of the magnetic vector potential u is discretized by a linear combination of the same scalar basis functions $w_j^{(q)}$ used for weighting and H_θ is expressed by a superposition of N_Γ harmonic basis functions [23] as

$$u^{(q)} \approx \sum_{j=1}^{N_q} u_j^{(q)} w_j^{(q)}, \quad H_\theta^{(q)}(\theta_q) \approx \sum_{k=1}^{N_\Gamma} \lambda_k^{(q)} e^{-\imath \ell_k \theta_q}, \tag{23}$$

where $\boldsymbol{\lambda}^{(q)} \in \mathbb{R}^{N_\Gamma}$ is the vector of Fourier coefficients for the harmonic basis functions, ℓ_k are the harmonic orders and $\mathbf{u}^{(q)} \in \mathbb{R}^{N_q}$ is the vector of degrees of freedom for each domain. This allows for a more efficient simulation of angular displacements $\alpha = \theta_{\mathrm{st}} - \theta_{\mathrm{rt}}$ when compared to classical mortaring, moving-band or sliding-surface methods [24]. Note that $u(\alpha) = u(x, y; \alpha)$ with $(x, y) \in D$, and the degrees of freedom $\mathbf{u}^{(q)}(\alpha)$ depend on the rotor position. The approach of harmonic stator-rotor coupling in an IGA framework leads to the Mortar-type saddle-point problem [19],

$$\begin{bmatrix} \mathbf{K}_{\mathrm{st}} & 0 & -\mathbf{G}_{\mathrm{st}}\mathbf{R}(\alpha) \\ 0 & \mathbf{K}_{\mathrm{rt}} & \mathbf{G}_{\mathrm{rt}} \\ -\mathbf{R}(\alpha)\mathbf{G}_{\mathrm{st}}^H & \mathbf{G}_{\mathrm{rt}}^H & 0 \end{bmatrix} \begin{bmatrix} \mathbf{u}^{(\mathrm{st})} \\ \mathbf{u}^{(\mathrm{rt})} \\ \boldsymbol{\lambda} \end{bmatrix} = \begin{bmatrix} \mathbf{j}_{\mathrm{st}} \\ \mathbf{j}_{\mathrm{rt}} \\ 0 \end{bmatrix}. \tag{24}$$

Here, $\boldsymbol{\lambda} = \boldsymbol{\lambda}^{(\mathrm{st})} = \boldsymbol{\lambda}^{(\mathrm{rt})}$ is enforced strongly by testing with $v = w$, $\mathbf{K}_q \in \mathbb{R}^{N_q \times N_q}$ are the stiffness matrices with

$$(\mathbf{K}_q)_{ij} = \int_{D_q} \left(\nu \frac{\partial w_i}{\partial x}\frac{\partial w_j}{\partial x} + \nu \frac{\partial w_i}{\partial y}\frac{\partial w_j}{\partial y}\right) \mathrm{d}D_q, \tag{25}$$

$\mathbf{G}_q \in \mathbb{C}^{N_q \times N_\Gamma}$ are the coupling matrices with

$$(\mathbf{G}_{\mathrm{st}})_{ik} = -\int_0^{2\pi} e^{-\imath \ell_k \theta_{\mathrm{st}}} w_i\left(\mathbf{r}\left(\theta_{\mathrm{st}}\right)\right) R_\Gamma \,\mathrm{d}\theta_{\mathrm{st}}, \tag{26}$$

$$(\mathbf{G}_{\mathrm{rt}})_{ik} = \int_0^{2\pi} e^{-\imath \ell_k \theta_{\mathrm{rt}}} w_i\left(\mathbf{r}\left(\theta_{\mathrm{rt}}\right)\right) R_\Gamma \,\mathrm{d}\theta_{\mathrm{rt}}, \tag{27}$$

where R_Γ is the radius of the interface Γ, $\mathbf{r}(\theta) = (R_\Gamma \cos(\theta), R_\Gamma \sin(\theta))^\top$ is a mapping from an angle θ to the point on the interface at this angle in Cartesian coordinates and $\mathbf{R}(\alpha) \in \mathbb{C}^{N_\Gamma \times N_\Gamma}$ is the diagonal rotation matrix with $(\mathbf{R}(\alpha))_{kk} = e^{\imath \ell_k \alpha}$. The saddle-point problem (24) is stable if the numbers N_q and N_Γ of basis functions are chosen consistently [19].

C. B-splines and NURBS

Isogeometric analysis is based on the idea of using freeform curves for an exact geometry representation of CAD models. This avoids errors in the geometry induced by mesh generation. For this, the notion of *B-splines*, i.e., piecewise polynomial functions, is of central importance. B-splines are defined via *knot vector* $\Xi = \{\xi_1, \xi_2, \ldots, \xi_{n+p+1}\}$ where the knots $\xi_i \in [0, 1]$ for all $i \in \{1, \ldots, n + p + 1\}$ are coordinates in the parametric space, p is the degree of the B-spline and n will be the dimension of the space. B-splines are defined by the recursive Cox-de Boor formula [25]

$$B_{i,p}(\xi) = \frac{\xi - \xi_i}{\xi_{i+p} - \xi_i} B_{i,p-1}(\xi) + \frac{\xi_{i+p+1} - \xi}{\xi_{i+p+1} - \xi_{i+1}} B_{i+1,p-1}(\xi), \tag{28}$$

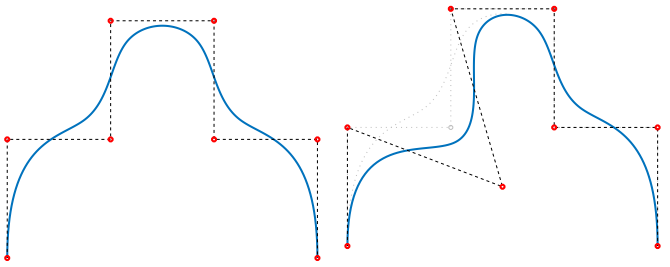

(a) Original NURBS curve.

(b) Modified NURBS curve where one control point is changed.

Fig. 3: Visualization of the modification of the shape of a NURBS curve by moving one control point.

for all $p \geq 1$ and for $p = 0$ via

$$B_{i,0}(\xi) = \begin{cases} 1 & \text{if } \xi_i \leq \xi < \xi_{i+1}, \\ 0 & \text{else,} \end{cases} \tag{29}$$

where $0/0 = 0$ is formally assumed. *NURBS* (Non-Uniform Rational B-splines) basis functions are then defined by

$$N_{i,p}(\xi) = \frac{w_i B_{i,p}(\xi)}{\sum_{k=1}^{n} w_k B_{k,p}(\xi)}, \tag{30}$$

where $w_k > 0$ for all $k = 1, 2, \ldots, n$ are so-called *weights*. NURBS curves can then be defined by the NURBS basis functions and control points $\mathbf{P}_i$ as

$$\mathbf{C}(\xi) = \sum_{i=1}^{n} \mathbf{P}_i N_{i,p}(\xi). \tag{31}$$

A NURBS curve can be locally modified by moving the control points. This is visualized in Fig. 3.

D. Isogeometric Analysis

Using the same functions for the representation of the geometry as in CAD software, i.e., NURBS, has the advantage that there is no need for the construction of a finite element geometry, i.e., the mesh. In isogeometric analysis the geometry is represented by a smooth mapping

$$\mathbf{F} : \hat{D} \to D, \tag{32}$$

using NURBS as basis functions, where $\hat{D}$ is the reference domain, i.e., in the 2D case the unit square, and D is the physical domain. The mapping $\mathbf{F}$ can be directly obtained from CAD software. However, not all geometries can be represented by a regular transformation of the reference domain $\hat{D} = [0,1]^n$, e.g., domains with a hole. In this case, a multipatch approach can be used to represent the physical domain. The physical domain D is subdivided into k patches D_k which can each be represented by a regular transformation of the reference domain $D_k = \mathbf{F}_k(\hat{D})$. A visualization is given in Fig. 4. The patches have a consistent discretization with a one-to-one matching of the degrees of freedom at the interfaces as in classical FEM, leading to a C^0 smoothness of the solution at the patch interfaces. Thus, the geometry of the CAD models can be exactly represented by a multipatch model [26] and there is no need for the generation of a computational

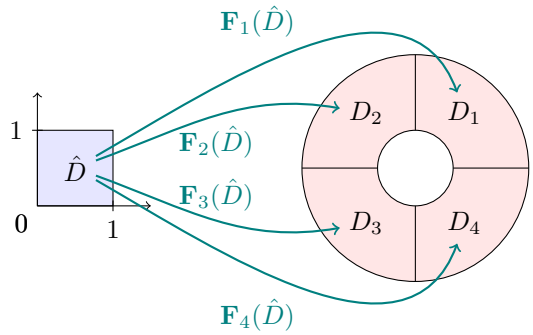

Fig. 4: Visualization of the mappings $\mathbf{F}_k$ from the reference domain $\hat{D}$ to the patches D_k of a multipatch geometry.

mesh that approximates the geometry, e.g., a triangulation. For the analysis, IGA uses the same setting as the classical finite element analysis with the exception of using B-splines or NURBS as basis and test functions w_j for $j = 1, \ldots, N_q$.

V. Numerical Shape Optimization

We solve the optimization problem (8)–(9) by means of a gradient-based shape optimization algorithm based on the shape derivative (20). By solving an auxiliary boundary value problem of the form

$$b(\mathbf{W}, \mathbf{Z}) = d\mathcal{J}(\Omega; \mathbf{Z}) \quad \forall \mathbf{Z} \tag{33}$$

with some positive definite bilinear form $b(\cdot, \cdot)$ satisfying $b(\mathbf{Z}, \mathbf{Z}) > 0$ for all vector fields $\mathbf{Z}$, we can extract a shape gradient $\mathbf{W}$, which satisfies $d\mathcal{J}(\Omega; \mathbf{W}) = b(\mathbf{W}, \mathbf{W}) > 0$. Thus, moving the control points of the motor geometry a small distance δ into the direction of $\mathbf{W}$ will yield an increase of the objective function $\mathcal{J}$. Likewise, since $d\mathcal{J}(\Omega; \mathbf{W})$ is linear in $\mathbf{W}$, a decrease can be achieved by moving the control points into the direction of the negative shape gradient $-\mathbf{W}$. The auxiliary boundary value problem (33) can be interpreted as finding a Riesz representative $\mathbf{W}$ of the functional $d\mathcal{J}(\Omega, \cdot)$ with respect to the metric given by $b(\cdot, \cdot)$. Of course, here different bilinear forms $b(\cdot, \cdot)$ can be chosen which amount to shape gradients in different metrics. In our algorithm, we choose

$$b(\mathbf{W}, \mathbf{Z}) = \int_D \mathbf{DW} : \mathbf{DZ} + \mathbf{W} \cdot \mathbf{Z} \, \mathrm{d}x \tag{34}$$

where we used $\mathbf{A} : \mathbf{B} = \sum_{i,j=1}^{n} A_{ij} B_{ij}$ denotes the Frobenius inner product for two matrices $\mathbf{A}, \mathbf{B} \in \mathbb{R}^n$ and $\mathbf{DW}$, $\mathbf{DZ}$ denote the Jacobi matrices of $\mathbf{W}$, $\mathbf{Z}$, respectively. Our algorithm consists in iteratively determining a descent vector field $\mathbf{W}$ by solving the auxiliary boundary value problem (33) with the bilinear form $b(\cdot, \cdot)$ given by (34) and moving the domain a distance δ into this direction. The step size δ is chosen as the maximum of the set $\{1, 1/2, 1/4, \ldots\}$ such that, no intersections of the patches occur and the objective value is decreased. When no further improvement can be achieved, the algorithm terminates. An overview of the shape optimization algorithm is given in Fig. 5.

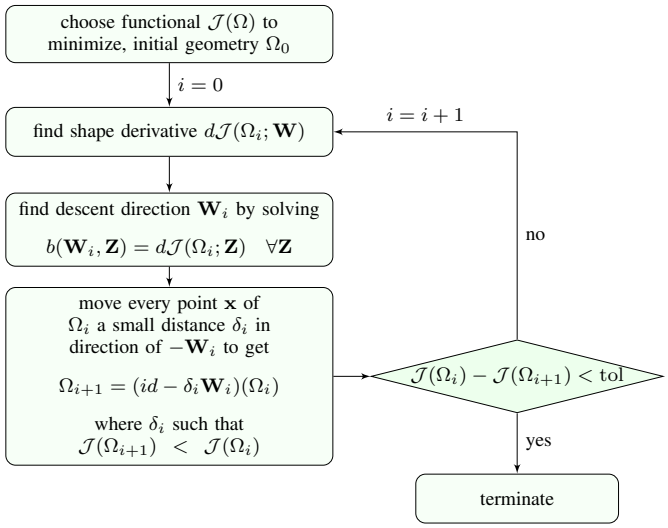

Fig. 5: Overview of the shape optimization algorithm.

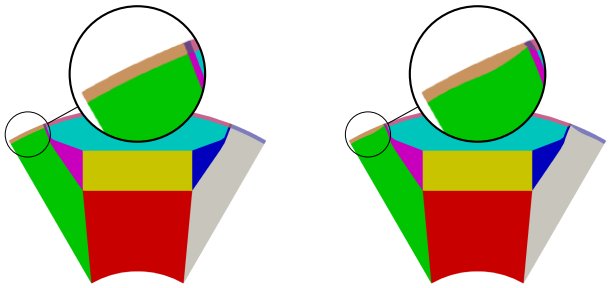

(a) Original design of the machine. (b) Optimized design of the machine.

Fig. 6: Results of shape optimization (8) in generator mode under no load condition. The shape of the rotor was optimized, minimizing the total harmonic distortion. Shape and position of the permanent magnet was fixed. Figure (a) shows the original design, figure (b) shows the optimized design.

VI. Results and Conclusion

The method described in Section V is used to minimize the total harmonic distortion by shape optimizing the rotor of a 6-pole permanent magnet synchronous machine (for the description of geometry and materials see [27, Chapter V.A]) in generator mode under no load condition. The shape and position of the permanent magnets in the rotor are fixed. The original and optimized design of the rotor can be seen in Fig. 6. The total harmonic distortion is reduced by more than $10\,\%$ in 60 iterations. The total harmonic distortion in the iterations of the shape optimization algorithm and the Fourier coefficients of the original design compared to the Fourier coefficients of the optimized design can be seen in Fig. 7.

In further works we will investigate the shape optimization for the machine in motor mode under load conditions. Furthermore, we will also consider non-linear materials in the machine and extend the machine model to three dimensions.

Acknowledgements

This work is supported by the German BMBF by the PASIROM project (grant nr. 05M2018RDA), the 'Excellence Initiative' of the German Federal and State Governments and by the Graduate School of Computational Engineering at Technische Universität Darmstadt. The authors thank H. De Gersem, Z. Bontinck and J. Corno for their help and the fruitful discussions.

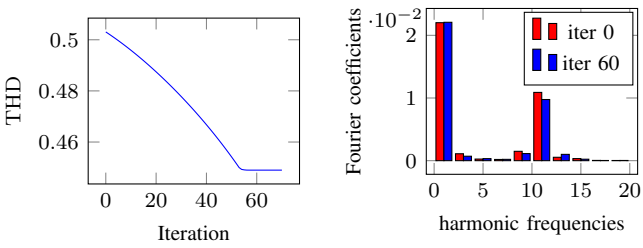

(a) Total harmonic distortion for each iteration of the shape optimization.

(b) Fourier coefficients for the original design in red and for the optimized design after 60 iterations in blue.

Fig. 7: Results of shape optimization (8) in generator mode under no load condition. The total harmonic distortion was reduced by more than $10\,\%$. Figure (a) shows the total harmonic distortion during the shape optimization, figure (b) shows the Fourier coefficients for the original and the optimized design.

References

[1] T. J. R. Hughes, J. A. Cottrell, and Y. Bazilevs, "Isogeometric analysis: CAD, finite elements, NURBS, exact geometry and mesh refinement," *Comput. Meth. Appl. Mech. Eng.*, vol. 194, pp. 4135–4195, 2005.

[2] A. Buffa, G. Sangalli, and R. Vázquez, "Isogeometric analysis in electromagnetics: B-splines approximation," *Comput. Meth. Appl. Mech. Eng.*, vol. 199, pp. 1143–1152, 2010.

[3] Z. Bontinck, J. Corno, H. De Gersem, S. Kurz, A. Pels, S. Schöps, F. Wolf, C. de Falco, J. Dölz, R. Vázquez, and U. Römer, "Recent advances of isogeometric analysis in computational electromagnetics," *ICS Newsletter (International Compumag Society)*, vol. 3, Nov. 2017.

[4] J. Dölz, H. Harbrecht, S. Kurz, S. Schöps, and F. Wolf, "A fast isogeometric BEM for the three dimensional Laplace- and Helmholtz problems," *Comput. Meth. Appl. Mech. Eng.*, vol. 330, pp. 83–101, Mar. 2018.

[5] P. Gangl, U. Langer, A. Mantzaflaris, and R. Schneckenleitner, *Isogeometric simulation and shape optimization with applications to electrical machines*, ArXiv e-print, 2018.

[6] P. Di Barba, *Multiobjective Shape Design in Electricity and Magnetism*, ser. Lecture Notes in Electrical Engineering. Springer, 2010.

[7] Y. Duan and D. M. Ionel, "A review of recent developments in electrical machine design optimization methods with a permanent-magnet synchronous motor benchmark study," *IEEE Trans. Ind. Appl.*, vol. 49, no. 3, pp. 1268–1275, May 2013.

[8] S. Russenschuck, "Mathematical optimization techniques for the design of permanent magnet synchronous machines based on numerical field calculation," *IEEE Trans. Magn.*, vol. 26, no. 2, pp. 638–641, Mar. 1990.

[9] K. Weeber and S. R. H. Hoole, "Geometric parametrization and constrained optimization techniques in the design of salient pole synchronous machines," *IEEE Trans. Magn.*, vol. 28, no. 4, pp. 1948–1960, Jul. 1992.

[10] N. Takorabet, B. Laporte, and G. Vinsard, "On the optimization of linear induction devices," *Electr. Eng.*, vol. 80, pp. 221–226, 1997.

[11] K. Hameyer and M. Kasper, "Shape optimization of a fractional horse-power DC-motor by stochastic methods," in *Computer Aided Optimimum Design of Structures III: Optimization of Structural Systems and Applications*, S. Hernandez and C. Brebbia, Eds., 1993, pp. 15–30.

[12] C. L. Lok, B. Vengadaesvaran, and S. Ramesh, "Implementation of hybrid pattern search–genetic algorithm into optimizing axial-flux permanent magnet coreless generator (AFPMG)," *Electr. Eng.*, vol. 99, pp. 751–761, 2017.

[13] C. Ma and L. Qu, "Multiobjective optimization of switched reluctance motors based on design of experiments and particle swarm optimization," *IEEE Trans. Energ. Convers.*, vol. 30, no. 3, pp. 1144–1153, Sep. 2015.

[14] U. Baumgartner, C. Magele, and W. Renhart, "Pareto optimality and particle swarm optimization," *IEEE Trans. Magn.*, vol. 40, no. 2, p. 1172, Mar. 2004.

[15] S. L. Ho, S. Yang, L. E. W. C. Ni Guangzheng, and H. C. Wong, "A particle swarm optimization-based method for multiobjective design optimizations," *IEEE Trans. Magn.*, vol. 41, no. 5, pp. 1756–1759, May 2005.

[16] B. N. Cassimere and S. D. Sudhoff, "Population-based design of surface-mounted permanent-magnet synchronous machines," *IEEE Trans. Energ. Convers.*, vol. 24, no. 2, pp. 338–346, Jun. 2009.

[17] M. L. Bash and S. D. Pekarek, "Modeling of salient-pole wound-rotor synchronous machines for population-based design," *IEEE Trans. Energ. Convers.*, vol. 26, no. 2, pp. 381–392, Jun. 2011.

[18] G. Y. Sizov, P. Zhang, D. M. Ionel, N. A. O. Demerdash, and M. Rosu, "Automated multi-objective design optimization of PM AC machines using computationally efficient FEA and differential evolution," *IEEE Trans. Ind. Appl.*, vol. 49, no. 5, pp. 2086–2096, Sep. 2013.

[19] Z. Bontinck, J. Corno, S. Schöps, and H. De Gersem, "Isogeometric analysis and harmonic stator-rotor coupling for simulating electric machines," *Comput. Meth. Appl. Mech. Eng.*, vol. 334, pp. 40–55, 2018.

[20] S. Schöps, H. De Gersem, and T. Weiland, "Winding functions in transient magnetoquasistatic field-circuit coupled simulations," *COMPEL*, vol. 32, no. 6, pp. 2063–2083, Sep. 2013.

[21] P. Gangl, U. Langer, A. Laurain, H. Meftahi, and K. Sturm, "Shape optimization of an electric motor subject to nonlinear magnetostatics," *SIAM J. Sci. Comput.*, vol. 37, no. 6, B1002–B1025, 2015.

[22] P. Hansbo, C. Lovadina, I. Perugia, and G. Sangalli, "A lagrange multiplier method for the finite element solution of elliptic interface problems using non-matching meshes," *Numer. Math.*, vol. 100, no. 1, pp. 91–115, Mar. 2005.

[23] H. De Gersem and T. Weiland, "Harmonic weighting functions at the sliding interface of a finite-element machine model incorporating angular displacement," *IEEE Trans. Magn.*, vol. 40, no. 2, pp. 545–548, Mar. 2004.

[24] H. De Gersem, J. Gyselinck, P. Dular, K. Hameyer, and T. Weiland, "Comparison of sliding-surface and moving-band techniques in frequency-domain finite-element models of rotating machines," *COMPEL*, vol. 23, no. 4, pp. 1006–1014, 2004.

[25] L. Piegl and W. Tiller, *The NURBS Book*, 2nd ed. Springer, 1997.

[26] A. Buffa, R. H. Vázquez, G. Sangalli, and L. B. da Veiga, "Approximation estimates for isogeometric spaces in multipatch geometries," *Numer. Meth. Part. Differ. Equat.*, vol. 31, no. 2, pp. 422–438, 2015.

[27] Z. Bontinck, "Numerical methods for the estimation of the impact of geometric uncertainties on the performance of electromagnetic devices," Dissertation, Technische Universität Darmstadt, Darmstadt, Nov. 2018.

Erschienene Preprints ab Nummer 2015/1

2015/1 O. Steinbach: Space-time finite element methods for parabolic problems

2015/2 O. Steinbach, G. Unger: Combined boundary integral equations for acoustic scattering-resonance problems problems.

2015/3 C. Erath, G. Of, F.–J. Sayas: A non-symmetric coupling of the finite volume method and the boundary element method

2015/4 U. Langer, M. Schanz, O. Steinbach, W.L. Wendland (eds.): 13th Workshop on Fast Boundary Element Methods in Industrial Applications, Book of Abstracts

2016/1 U. Langer, M. Schanz, O. Steinbach, W.L. Wendland (eds.): 14th Workshop on Fast Boundary Element Methods in Industrial Applications, Book of Abstracts

2016/2 O. Steinbach: Stability of the Laplace single layer boundary integral operator in Sobolev spaces

2017/1 O. Steinbach, H. Yang: An algebraic multigrid method for an adaptive space-time finite element discretization

2017/2 G. Unger: Convergence analysis of a Galerkin boundary element method for electromagnetic eigenvalue problems

2017/3 J. Zapletal, G. Of, M. Merta: Parallel and vectorized implementation of analytic evaluation of boundary integral operators

2017/4 S. Dohr, O. Steinbach: Preconditioned space-time boundary element methods for the one-dimensional heat equation

2017/5 O. Steinbach, H. Yang: Comparison of algebraic multigrid methods for an adaptive space–time finite element discretization of the heat equation in 3D and 4D

2017/6 S. Dohr, K. Niino, O. Steinbach: Preconditioned space-time boundary element methods for the heat equation

2017/7 O. Steinbach, M. Zank: Coercive space-time finite element methods for initial boundary value problems

2017/8 U. Langer, M. Schanz, O. Steinbach, W.L. Wendland (eds.): 15th Workshop on Fast Boundary Element Methods in Industrial Applications, Book of Abstracts

2018/1 U. Langer, M. Schanz, O. Steinbach, W.L. Wendland (eds.): 16th Workshop on Fast Boundary Element Methods in Industrial Applications, Book of Abstracts

2018/2 S. Dohr, J. Zapletal, G. Of, M. Merta, M. Kravcenko: A parallel space-time boundary element method for the heat equation

2018/3 S. Dohr, M. Merta, G. Of, O. Steinbach, J. Zapletal: A parallel solver for a preconditioned space-time boundary element method for the heat equation

2018/4 S. Amstutz, P. Gangl: Toplogical derivative for nonlinear magnetostatic problem

2018/5 O. Steinbach, M. Zank: A Stabilized Space–Time Finite Element Method for the Wave Equation

2018/6 O. Steinbach, H. Yang: A Space-Time Finite Element Method for the Linear Bidomain Equations

2018/7 O. Steinbach, M. Zank: Coercive space-time finite element methods for initial boundary value problems

2018/8 S. Dohr, K. Niino, O. Steinbach: Space-time boundary element methods for the heat equation

2018/8 O. Steinbach, H. Yang: Space-time finite element methods for parabolic evolution equations: Discretization, a posteriori error estimation, adaptivity and solution

2019/1 O. Steinbach (eds.): 15th Austrian Numerical Analysis Day, Book of Abstracts

2019/2 P. Gangl, K. Sturm: A simplified derivation technique of topological derivatives for quasi-linear transmission problems